The Astrophysical Journal, 604:766–774, 2004 April 1

WARPING AND PRECESSION OF ACCRETION DISKS AROUND MAGNETIC STARS: NONLINEAR EVOLUTION

Harald P. Pfeiffer[1] and Dong Lai
Center for Radiophysics and Space Research, Cornell University, Ithaca, NY 14853; harald@astro.cornell.edu, dong@astro.cornell.edu
Received 2003 July 16; accepted 2003 December 11

ABSTRACT

The inner region of the accretion disk around a magnetized star (T Tauri star, white dwarf, or neutron star) is subjected to magnetic torques that induce warping and precession of the disk. These torques arise from the interaction between the stellar field and the induced electric currents in the disk. We carry out numerical simulations of the nonlinear evolution of warped, viscous accretion disks driven by the magnetic torques. We show that the disk can develop into a highly warped steady state in which the disk attains a fixed (warped) shape and precesses rigidly. The warp is most pronounced at the disk inner radius (near the magnetosphere boundary). As the system parameters (such as accretion rate) change, the disk can switch between a completely flat state (warping-stable) and a highly warped state. The precession of warped disks may be responsible for a variety of quasi-periodic oscillations or radiation flux variabilities observed in many different systems, including young stellar objects and X-ray binaries.

Subject headings: accretion, accretion disks — binaries: general — stars: magnetic fields — stars: neutron — stars: pre–main-sequence

1. INTRODUCTION

Warped accretion disks are believed to exist in a variety of astrophysical systems, including X-ray binaries, young stellar objects (YSOs), and active galactic nuclei. For example, the well-known 164 day precession of the jet in SS 433 and the long-term variabilities observed in many X-ray binaries (e.g., Her X-1 and LMC X-4; see Priedhorsky & Holt 1987; Scott et al. 2000; Ogilvie & Dubus 2001) have been explained by the precession of tilted accretion disks. The changes in the flow directions of several YSO jets (e.g., Bate et al. 2000) and the photometric variabilities of some T Tauri stars (e.g., AA Tauri; see Bouvier et al. 1999; Carpenter, Hillenbrand, & Skrutskie 2001) have also been associated with warped, precessing disks.

Several mechanisms for exciting/maintaining warps in accretion disks have been proposed in recent years. Schandl & Meyer (1994) considered a warping instability due to irradiation-driven disk wind. Pringle (1996) showed that even without wind loss, radiation pressure itself can induce warping in the outer region of the disk (see also Maloney, Begelman, & Nowak 1998; Wijers & Pringle 1999; Ogilvie & Dubus 2001). Quillen (2001) showed that a wind passing over the disk surface may induce warping via Kelvin-Helmholtz instability. Finally, in the case of disk accretion onto magnetic stars (e.g., neutron stars, white dwarfs, and T Tauri stars), the stellar magnetic field can induce disk warping and precession (Lai 1999; see also Terquem & Papaloizou 2000). In this paper we are concerned with these magnetic effects on accretion disks.

The study of disk accretion onto magnetic stars has a long history (e.g., Pringle & Rees 1972; Ghosh & Lamb 1979; Anzer & Börner 1980, 1983; Lipunov & Shakura 1980; Wang 1987, 1995; Aly & Kuijpers 1990; Spruit & Taam 1993; Shu et al. 1994; van Ballegooijen 1994; Lovelace, Romanova, & Bisnovatyi-Kogan 1995, 1999; Campbell 1997; Lai 1998; see also numerical simulations by Hayashi, Shibata, & Matsumoto 1996; Miller & Stone 1997; Goodson, Winglee, & Böhm 1997; Fendt & Elstner 2000; Romanova et al. 2003). Most previous studies have, for simplicity, adopted the idealized geometry in which the magnetic axis, the spin axis, and the disk angular momentum are aligned. However, it was shown in Lai (1999) that under quite general conditions, the stellar magnetic field can induce warping in the inner disk and make the disk precess around the spin axis (see § 2; see also Aly 1980; Lipunov & Shakura 1980; Terquem & Papaloizou 2000). Such magnetically driven warping and precession open up new possibilities for the dynamical behaviors of disk accretion onto magnetic stars. Shirakawa & Lai (2002a) studied these effects in weakly magnetized accreting neutron stars and showed that the magnetic warping/precession effects may explain several observed features of low-frequency quasi-periodic oscillations in low-mass X-ray binaries. Shirakawa & Lai (2002b) also studied the linear, global warping/precession modes of inner disks of highly magnetized ($B \sim 10^{12}$ G) neutron stars (NSs), as in accreting X-ray pulsars, and suggested that magnetically driven disk warping and precession can explain the mHz variabilities observed in X-ray pulsars.

The studies by Shirakawa & Lai (2002a, 2002b) were restricted to linear warping. Such linear analysis is only the first step toward understanding the observational manifestations of the magnetic warping/precession effects. However, as we show in this paper, under many circumstances, the disk warping becomes nonlinear, and the dynamics of nonlinear warped disks is much richer. This is the subject of this paper. After briefly reviewing the basic physics of magnetically driven disk warping and precession (§ 2), we present the dynamical equations for the warped disk (§ 3) and our numerical results (§ 4) and discuss their astrophysical implications (§ 5). The Appendix contains more details of our numerical method.

2. MAGNETICALLY DRIVEN DISK WARPING/PRECESSION

For completeness, we briefly review the basic physics of magnetically driven warping/precession and give the formulae to be used in later sections.

[1] Current address: Theoretical Astrophysics, MS 130-33, California Institute of Technology, Pasadena, CA 91125.

The inner region of the accretion disk onto a rotating magnetized central star is subjected to magnetic torques that induce warping and precession of the disk (Lai 1999). These magnetic torques result from the interactions between the accretion disk and the stellar magnetic field. Depending on how the disk responds to the stellar field, two different kinds of torque arise: (1) If the vertical stellar magnetic field B_z penetrates the disk, it gets twisted by the disk rotation to produce an azimuthal field $\Delta B_\phi = \mp\zeta B_z$ that has different signs above and below the disk (ζ is the azimuthal pitch of the field line and depends on the dissipation in the disk), and a radial surface current K_r results. The interaction between K_r and the stellar B_ϕ gives rise to a vertical force. While the mean force (averaging over the azimuthal direction) is zero, the uneven distribution of the force induces a net *warping torque*, which tends to misalign the angular momentum of the disk with the stellar spin axis. (2) If the disk does not allow the vertical stellar field (e.g., the rapidly varying component of B_z due to stellar rotation) to penetrate, an azimuthal screening current K_ϕ will be induced on the disk. This K_ϕ interacts with the radial magnetic field B_r and produces a vertical force. The resulting *precessional torque* tends to drive the disk into retrograde precession around the stellar spin axis.

In general, both the magnetic warping torque and the precessional torque are present. For small disk tilt angle β (the angle between the disk normal and the spin axis), the precession angular frequency and warping rate at radius r are given by (Lai 1999)

$$\Omega_p(r) = \frac{\mu^2}{\pi^2 r^7 \Omega(r)\Sigma(r) D(r)} F(\theta), \tag{1}$$

$$\Gamma_w(r) = \frac{\zeta\mu^2}{4\pi r^7 \Omega(r)\Sigma(r)} \cos^2\theta, \tag{2}$$

where μ is the stellar magnetic dipole moment, θ is the angle between the magnetic dipole axis and the spin axis, $\Omega(r)$ is the orbital angular frequency, and $\Sigma(r)$ is the surface density of the disk. The dimensionless function $D(r)$ is given by

$$D(r) = \max\left[\sqrt{r^2/r_{\rm in}^2 - 1},\ \sqrt{2H(r)/r_{\rm in}}\right]. \tag{3}$$

Here $H(r)$ is the half-thickness of the disk, and $r_{\rm in}$ is the inner disk radius, given by the magnetosphere radius

$$r_{\rm in} \equiv \eta\left(\frac{\mu^4}{GM\dot{M}^2}\right)^{1/7}, \tag{4}$$

where M is the stellar mass, $\dot{M}$ is the mass accretion rate, and $\eta \sim 0.5$–1. The function $F(\theta)$ depends on the dielectric property of the disk. We can write

$$F(\theta) = 2f\cos^2\theta - \sin^2\theta, \tag{5}$$

so that $F(\theta) = -\sin^2\theta$ if only the spin-variable vertical field is screened out by the disk ($f = 0$), and $F(\theta) = 3\cos^2\theta - 1$ if all vertical field is screened out ($f = 1$). In reality, f lies between 0 and 1. For concreteness, we set $F(\theta) = -\sin^2\theta$ in the following.

3. DYNAMICAL EQUATIONS FOR WARPED DISKS

In a viscous accretion disk (with the dimensionless viscosity parameter $\alpha \gtrsim H/r$), the dynamics of the disk warp is dominated by viscous stress (rather than bending waves; see Papaloizou & Lin 1995; Terquem 1998) and can be studied using the formalism of Papaloizou & Pringle (1983) (see also Pringle 1992; Ogilvie 1999; Ogilvie & Dubus 2001). We model the disk as a collection of rings that interact with each other via viscous stresses. Each ring at radius r has the unit normal vector $\hat{\boldsymbol{l}}(r, t)$. In Cartesian coordinates, with the z-axis along the stellar spin $\hat{\boldsymbol{\omega}}$, we can write

$$\hat{\boldsymbol{l}} = \begin{pmatrix} \sin\beta\cos\gamma \\ \sin\beta\sin\gamma \\ \cos\beta \end{pmatrix}, \tag{6}$$

with $\beta(r, t)$ the tilt angle and $\gamma(r, t)$ the twist angle. The relevant equations are mass conservation,

$$\frac{\partial\Sigma}{\partial t} + \frac{1}{r}\frac{\partial}{\partial r}(r\Sigma V_r) = 0, \tag{7}$$

and the evolution equation for $\hat{\boldsymbol{l}}$,

$$\frac{\partial\hat{\boldsymbol{l}}}{\partial t} + \left[V_r - \frac{\nu_1(\partial\Omega/\partial r)}{\Omega} - \frac{1}{2}\nu_2\frac{\partial(\Sigma r^3\Omega)/\partial r}{\Sigma r^3\Omega}\right]\frac{\partial\hat{\boldsymbol{l}}}{\partial r} = \frac{\partial}{\partial r}\left(\frac{1}{2}\nu_2\frac{\partial\hat{\boldsymbol{l}}}{\partial r}\right) + \frac{1}{2}\nu_2\left|\frac{\partial\hat{\boldsymbol{l}}}{\partial r}\right|^2\hat{\boldsymbol{l}} + \frac{\boldsymbol{N}}{\Sigma r^2\Omega}. \tag{8}$$

Here ν_1 is the usual disk viscosity (measuring the r-ϕ stress), ν_2 denotes the viscosity of the r–z stress that is associated with reducing the disk tilt, and $\boldsymbol{N}$ represents external torques acting on the disk. The radial velocity was derived by Pringle (1992):

$$V_r = \frac{(\partial/\partial r)[\nu_1\Sigma r^3(\partial\Omega/\partial r)]}{r\Sigma\partial(r^2\Omega)/\partial r} - \frac{\nu_2}{2}\frac{r^2\Omega}{\partial(r^2\Omega)/\partial r}\left|\frac{\partial\hat{\boldsymbol{l}}}{\partial r}\right|^2. \tag{9}$$

The nonlinear warp equation (8) is based on a phenomenological description of the viscosities ν_1 and ν_2 and is formally valid only in the linear regime when the local disk warp $\partial\hat{\boldsymbol{l}}/\partial\ln r$ is small (Ogilvie 1999). A more rigorous treatment by Ogilvie (1999) removes this assumption and finds that ν_1 and ν_2 effectively depend on the warp amplitude $\partial\hat{\boldsymbol{l}}/\partial\ln r$. Ogilvie (1999) also finds an additional term causing dispersive propagation and precession. However, it turns out that this latter term is not very important for Keplerian disks. For the current investigation into the qualitative features of the magnetic warping and precession instability we adopt the simpler equations given by Pringle (1992).

The torque $\boldsymbol{N}$ in equation (8) was derived in Lai (1999) as

$$\frac{\boldsymbol{N}}{\Sigma r^2\Omega} = \Omega_p\cos\beta\hat{\boldsymbol{\omega}}\times\hat{\boldsymbol{l}} - \Gamma_w\cos\beta\left[\hat{\boldsymbol{\omega}} - (\hat{\boldsymbol{\omega}}\cdot\hat{\boldsymbol{l}})\hat{\boldsymbol{l}}\right], \tag{10}$$

where Ω_p and Γ_w are given by equations (1) and (2). The first term of equation (10) causes retrograde precession of the tilted disk [since $\Omega_p < 0$ because of the choice $F(\theta) = -\sin^2\theta$], whereas the second term tries to warp the disk.

The magnetic torque formulae (eqs. [1] and [2]) contain uncertain parameters (e.g., ζ, which parameterizes the amount of azimuthal twist of the magnetic field threading the disk); this is inevitable given the complicated nature of magnetic field–disk interaction (see Lai 1999 and references therein). In addition, while the expression for the warping torque (eq. [2]) is formally valid for large disk warps, the expression for the

precession torque was derived under the assumption that the disk is locally flat (eq. [1] is strictly valid only for a completely flat disk; Aly 1980); when this assumption breaks down (i.e., when $\partial\hat{\boldsymbol{l}}/\partial \ln r$ is large), we expect a similar torque expression to hold, but with modified numerical factors [e.g., the function $D(r)$ in eq. (1) will be different]. When an almost flat disk becomes unstable to the warping instability, and also in the deeply nonlinear warp regime with disk tilted to large radii (see § 4), the condition $|\partial\hat{\boldsymbol{l}}/\partial \ln r| \lesssim 1$ is well satisfied. Thus, we believe that our simplifying assumptions capture the qualitative behavior of accretion disks subject to the magnetic torques.

3.1. *Boundary Conditions*

We need boundary conditions for $\hat{\boldsymbol{l}}$ and for the surface density Σ. The torque (eq. [10]) decays rapidly with radius, so that we expect the outer disk to be undisturbed. This is confirmed by the linear stability analysis of Shirakawa & Lai (2002a, 2002b). We therefore adopt simple Dirichlet boundary conditions at the outer edge of the disk,

$$\hat{\boldsymbol{l}}(r_{\rm out}) \equiv \hat{\boldsymbol{l}}_{\rm out} = {\rm const.} \tag{11}$$

Throughout this paper we choose $\hat{\boldsymbol{l}}_{\rm out} = \hat{\boldsymbol{\omega}}$, such that the outer disk is perpendicular to the rotation axis of the star. At the inner edge of the disk, we use a zero torque boundary condition,

$$\frac{\partial\hat{\boldsymbol{l}}}{\partial r}(r_{\rm in}) = 0. \tag{12}$$

The boundary condition on Σ is motivated by the flat Keplerian disk, which has[2]

$$\Sigma_{\rm flat} = \frac{\dot{M}}{3\pi\nu_1}\mathcal{J}, \tag{13}$$

with $\mathcal{J} = 1 - (1 - \mathcal{J}_{\rm in})(r/r_{\rm in})^{-1/2}$. We choose Dirichlet boundary conditions on the surface density,

$$\Sigma(r_{\rm out}) = \frac{\dot{M}}{3\pi\nu_1}\mathcal{J}_{\rm out}, \quad \Sigma(r_{\rm in}) = \frac{\dot{M}}{3\pi\nu_1}\mathcal{J}_{\rm in}, \tag{14}$$

where $\mathcal{J}_{\rm out} = 1 - (1 - \mathcal{J}_{\rm in})(r_{\rm out}/r_{\rm in})^{-1/2}$. We take $\mathcal{J}_{\rm in}$ to be free, parameterizing the physics at the inner edge of the disk.

3.2. *Dimensionless Equations*

The radius is measured in multiples of the radius of the inner edge, $x = r/r_{\rm in}$, and we introduce a dimensionless surface density $\sigma = \Sigma/\Sigma_0$. We assume viscosities of the form

$$\nu_1 = \nu_{10}x^{\beta_1}\sigma^{\sigma_1}, \quad \nu_2 = \nu_{20}x^{\beta_2}\sigma^{\sigma_2}. \tag{15}$$

In light of equation (13), we take $\Sigma_0 = \dot{M}/(3\pi\nu_{10})$. Finally, we measure time in units of the viscous timescale at the inner edge, $t = t_0\tau$, $t_0 = r_{\rm in}^2/\nu_{10}$, and define $\eta_0 = \nu_{20}/\nu_{10}$. With these assumptions, equations (7)–(9) simplify to

$$\frac{\partial\sigma}{\partial\tau} + \frac{1}{x}\frac{\partial}{\partial x}\left[\frac{\left(\sigma^{\sigma_1+1}x^{\beta_1+3}\Omega'\right)'}{\left(x^2\Omega\right)'} - \frac{\eta_0}{2}\sigma^{\sigma_2+1}\frac{x^{\beta_2+3}\Omega}{\left(x^2\Omega\right)'}\left|\hat{\boldsymbol{l}}'\right|^2\right] = 0, \tag{16}$$

$$\frac{\partial\hat{\boldsymbol{l}}}{\partial\tau} - \frac{\eta_0}{2}\sigma^{\sigma_2}x^{\beta_2}\left(\hat{\boldsymbol{l}}'' + \left|\hat{\boldsymbol{l}}'\right|^2\hat{\boldsymbol{l}}\right) + \left\{\frac{\left(\sigma^{\sigma_1+1}x^{\beta_1+3}\Omega'\right)'}{\sigma x\left(x^2\Omega\right)'} - \sigma^{\sigma_1}x^{\beta_1}\frac{\Omega'}{\Omega} - \frac{\eta_0}{2}\left[\frac{\left(\sigma^{\sigma_2+1}x^{\beta_2+3}\Omega\right)'}{\sigma x^3\Omega} + \sigma^{\sigma_2}\frac{x^{\beta_2+2}\Omega}{\left(x^2\Omega\right)'}\left|\hat{\boldsymbol{l}}'\right|^2\right]\right\}\hat{\boldsymbol{l}}' = \boldsymbol{n}, \tag{17}$$

where a prime denotes $\partial/\partial x$. The dimensionless torque is given by

$$\boldsymbol{n} = \frac{t_0\boldsymbol{N}}{r^2\Sigma\Omega} = \frac{\hat{\boldsymbol{l}}\cdot\hat{\boldsymbol{\omega}}}{\sigma x^{5.5}}\left\{-\frac{\bar{\Omega}_p}{D(x)}\hat{\boldsymbol{\omega}}\times\hat{\boldsymbol{l}} - \bar{\Gamma}_w\left[\hat{\boldsymbol{\omega}} - \left(\hat{\boldsymbol{\omega}}\cdot\hat{\boldsymbol{l}}\right)\hat{\boldsymbol{l}}\right]\right\}, \tag{18}$$

where

$$\bar{\Omega}_p = \frac{3}{\pi}\frac{\sin^2\theta}{\eta^{3.5}} = 5.4\left(\frac{\eta}{0.5}\right)^{-3.5}\left(\frac{\sin^2\theta}{0.5}\right), \tag{19}$$

$$\bar{\Gamma}_w = \frac{3}{4}\eta^{-3.5}\zeta\cos^2\theta = 21\left(\frac{\eta}{0.5}\right)^{-3.5}\left(\frac{\zeta}{5}\right)\left(\frac{\cos^2\theta}{0.5}\right), \tag{20}$$

are dimensionless constants independent of r and t, parameterizing the problem. We first set $D(x) = 1$ to make contact with the linear stability analysis in Shirakawa & Lai (2002b). Later in this paper, we use equation (3) and set for concreteness $H(r)/r_{\rm in} = 0.02$ close to the inner edge, so that

$$D(x) = \max\left(\sqrt{x^2 - 1},\ 0.2\right). \tag{21}$$

[The specific choice of $D(x)$ influences our qualitative results only marginally, as the radial dependence of the precession torque in eq. (1) is dominated by the r^{-7} piece.]

While equations (16) and (17) can be applied for a general viscosity law (eq. [15]), in our calculations we restrict to the cases where $\nu_2/\nu_1 = \nu_{20}/\nu_{10} = \eta_0$. The ratio η_0 measures the disk's resistance to warping; we consider different values of η_0, ranging from $\eta_0 = 1$ to $\eta_0 \gg 1$.[3]

Finally, we give the boundary conditions in dimensionless variables:

$$\frac{\partial\hat{\boldsymbol{l}}}{\partial x}(x_{\rm in}) = 0, \quad \hat{\boldsymbol{l}}(x_{\rm out}) = \hat{\boldsymbol{l}}_{\rm out}, \tag{22}$$

$$\sigma(x_{\rm in}) = \sigma_{\rm flat}(x_{\rm in}), \quad \sigma(x_{\rm out}) = \sigma_{\rm flat}(x_{\rm out}), \tag{23}$$

where, by definition, $x_{\rm in} = 1$, and $\sigma_{\rm flat} \equiv \Sigma_{\rm flat}/\Sigma_0$ follows from equations (13) and (15):

$$\sigma_{\rm flat} = \left\{\left[1 - (1 - \mathcal{J}_{\rm in})x^{-1/2}\right]x^{-\beta_1}\right\}^{1/(1+\sigma_1)}. \tag{24}$$

4. NUMERICAL RESULTS

Equations (16) and (17) with boundary conditions given by equations (22) and (23) are solved with a Crank-Nicholson scheme as described in the Appendix.

[2] This expression for $\Sigma_{\rm flat}$ applies to a nonmagnetic disk. When magnetic fields thread the disk, the functional form of $\mathcal{J}(r)$ is modified in a model-dependent way (see Appendix A of Lai 1999 for examples).

[3] For a Keplerian disk, assuming isotropic viscous stress parameterized by the α *Ansatz*, the ratio ν_2/ν_1 is of order $1/(2\alpha^2)$ for linear warps (Papaloizou & Pringle 1983; Ogilvie 1999). The large ν_2/ν_1 (for $\alpha \ll 1$) is due to the fact that horizontal motions induced in the disk by the warp are resonantly driven. Such resonant behavior tends to be diminished in the nonlinear regime and also when deviation from Keplerian rotation is present (Ogilvie 1999).

4.1. *Evolution into the Nonlinear Regime*

We first consider an almost flat, unstable disk, which we follow through the linear growth of the warping mode into the nonlinear regime. The particular parameters we use are $\bar{\Omega}_p = 10$, $\bar{\Gamma}_w = 10$, $\mathcal{J}_{\rm in} = 1$, $\eta_0 = 1$, $\beta_1 = \beta_2 = 0.6$, and $\sigma_1 = \sigma_2 = 0$, and we set $D(x) = 1$. The linear stability analysis for these parameters was presented in Shirakawa & Lai (2002b), where the disk was found to be unstable to the magnetic warping instability. As initial conditions for the evolution we take $|\sigma(x)|_{\tau=0} = \sigma_{\rm flat}(x)$, and perturb $\hat{\boldsymbol{l}}$ by $\sim 10^{-5}$ degrees away from $\hat{\boldsymbol{\omega}}$.

Figure 1 presents the tilt angle at the inner edge, $\beta_{\rm in} = \beta(x_{\rm in})$, and the precession frequency at the inner edge, $d\gamma_{\rm in}/d\tau$, as functions of time τ. The disk is indeed unstable, and a growing mode emerges. At early times, the tilt angle grows exponentially with e-folding time of $T_{e\text{-fold}} = (d \log \beta_{\rm in}/d\tau)^{-1} = 0.59$ and precession frequency $d\gamma_{\rm in}/d\tau = -4.22$. These numbers agree very well with the linear stability analysis of Shirakawa & Lai (2002b). At late times the growth slows down, and the tilt angle saturates around $\beta(r_{\rm in}) \approx 75^\circ$. Eventually, the disk settles into a solution in which the whole disk precesses with uniform precession frequency; i.e., the tilt angle profile $\beta(r)$ is independent of time, whereas the twist angle increases linearly in time, $\gamma(r, \tau) = \gamma_0(r) + \boldsymbol{\omega}_p \tau$, with the precession frequency $\boldsymbol{\omega}_p \simeq -0.72$.

Figure 2 presents the tilt angle $\beta(r)$ as a function of radius at different times. One sees clearly that after the mode has saturated, the tilted region of the disk is larger than during the linear phase. The profiles of the tilt angle provide an explanation for the reduction of precession frequency as the disk enters the nonlinear regime: The precessional torque given by the first term of equation (18), is suppressed by the factor $\hat{\boldsymbol{l}} \cdot \hat{\boldsymbol{\omega}} = \cos\beta$. Furthermore, a more extended disk is involved, reducing the precession rate further. In the final steady state, the precession period is $P = 2\pi/|\boldsymbol{\omega}_p| = 8.7$, while the warp diffusion time $T_{\rm diff}$ is of order $|\partial \hat{\boldsymbol{l}}/\partial r|^{-2} \nu_2^{-1} \sim r^2/\nu_2 = x^{1.4}/\nu_{20}$ (in dimensionless units). The disk warp extents to $x \lesssim 3$ (see Fig. 2) so that $T_{\rm diff} \approx 4.7 < P$. Thus, the different parts of the warped disk can communicate with each other through viscous diffusion on a timescale shorter than the precession time, making rigid-body precession possible. In addition, both P and $T_{\rm diff}$ are much larger than the e-folding time $T_{e\text{-fold}} \approx 0.59$ of the growth of linear perturbations. The inequalities $T_{e\text{-fold}} < T_{\rm diff} < P$ hold for all evolutions presented in this paper.

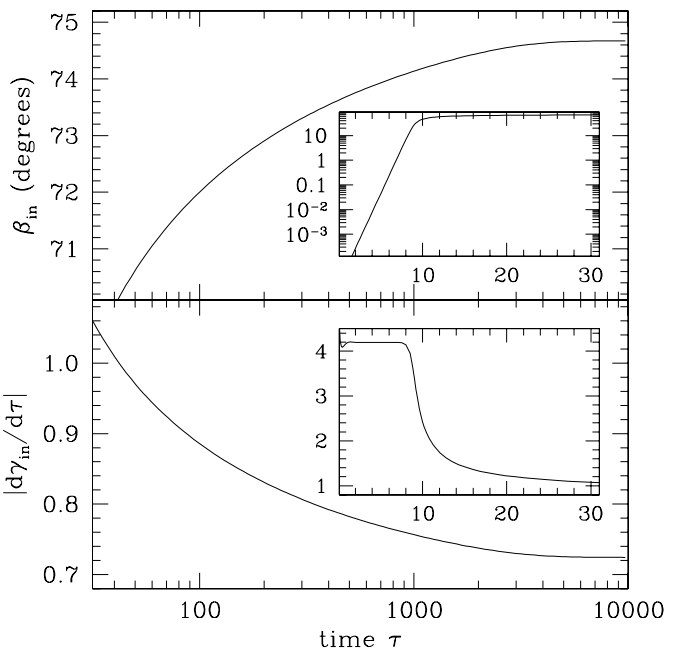

FIG. 1.—Tilt angle $\beta_{\rm in}$ at the inner edge and precession frequency at the inner edge during evolution into the nonlinear regime (parameters $\bar{\Omega}_p = \bar{\Gamma}_w = 10$, $\mathcal{J}_{\rm in} = 1$, $\eta_0 = 1$, $\beta_1 = \beta_2 = 0.6$, and $\sigma_1 = \sigma_2 = 0$.) The inserts show early times.

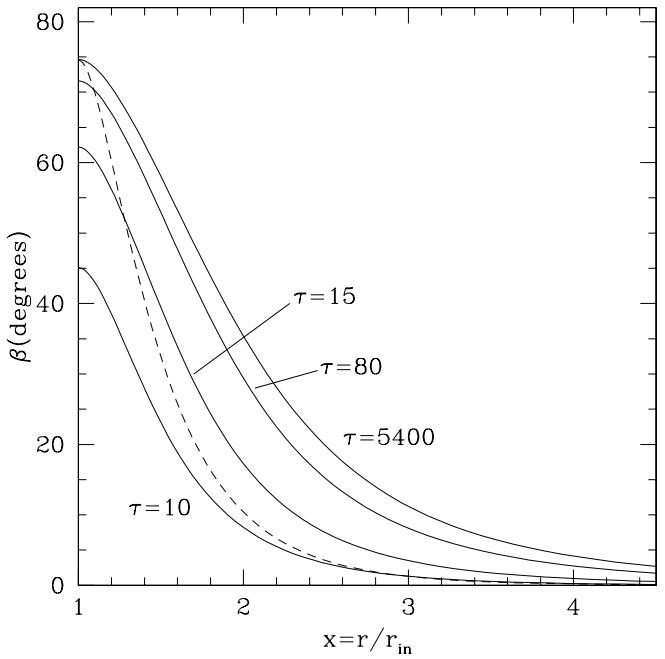

FIG. 2.—Tilt angle β as a function of radius at different times during the evolution presented in Fig. 1. The solid lines illustrate the growth of the warp; at $\tau = 5400$, the disk has essentially reached its final steady state. The dashed line represents the shape during the linear regime ($\tau = 6$, rescaled to coincide with the steady state solution at the inner edge), which agrees well with the eigenvector of the linear stability analysis of Shirakawa & Lai (2002b).

Figure 3 shows the surface density relative to the flat disk, $\sigma/\sigma_{\rm flat}$, at different times. As the evolution proceeds, the disk gets depleted. The reason for this is that as the disk warps, the second term in equation (9) gives rise to increased advection relative to the flat disk. Although the disk tilt is confined to relatively small radii (e.g., $\beta < 2^\circ$ for $x \gtrsim 5$, β decreases exponentially with larger x), the surface density is depleted over a larger region with the deviation from $\sigma_{\rm flat}$ decreasing only as $x^{-1/2}$. The outer disk depletes on the viscous timescale of the *outer* disk; this explains the very slow relaxation to the steady state in Figure 1. The fact that σ changes at large radii necessitates the use of a large computational domain, although the disk is only warped in the inner region. We typically place the outer boundary at $x_{\rm out} = 1000$, which results in accuracy of about 1%.

4.2. *Nonlinear Steady State of Warped Disk*

The growing mode is only a transient phenomenon—one will most likely observe only the nonlinear steady state solution. Therefore, we now study the properties of the steady state solution as a function of four of the parameters that characterize the system: $\bar{\Gamma}_w$, $\bar{\Omega}_p$, $\mathcal{J}_{\rm in}$, and η_0 (for definiteness, the other parameters are fixed, as in § 4.1).

First we consider the effect of varying $\bar{\Gamma}_w$ [keeping $\bar{\Omega}_p = 10$, $\mathcal{J}_{\rm in} = 1$, and $\eta_0 = 1$ and setting $D(x) = 1$, as in § 4.1]. For different $\bar{\Gamma}_w$, we perform evolutions until relaxation to steady

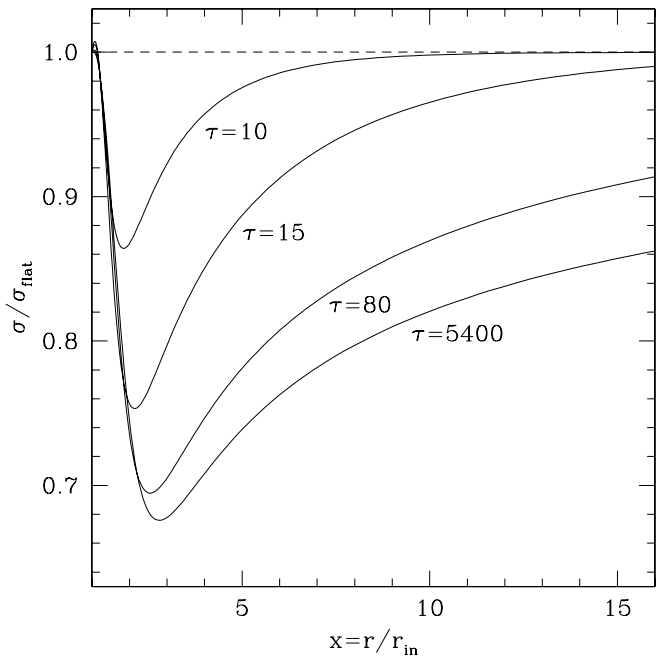

FIG. 3.—Surface density relative to the unperturbed, flat disk at different times during the evolution presented in Fig. 1. The dashed line represents our initial condition, $\sigma/\sigma_{\rm flat} \equiv 1$.

state, and then record the tilt angle $\beta_{\rm in}$ and the disk precession frequency $\boldsymbol{\omega}_p = d\boldsymbol{\gamma}_{\rm in}/d\tau$. Figure 4 presents the results of this computation. For $\bar{\Gamma}_w \gtrsim 6.2$, the disk is unstable to the magnetic warping instability (in agreement with the linear stability analysis); with increasing torque $\bar{\Gamma}_w$, the steady state tilt angle $\beta_{\rm in}$ increases. There is only a small window of torque parameters, for which the steady state disk is moderately warped (say, $0 < \beta_{\rm in} < 60^\circ$). Hence, this computation suggests that, whenever the magnetic warping instability operates, it is likely that the inner disk will be significantly tilted.

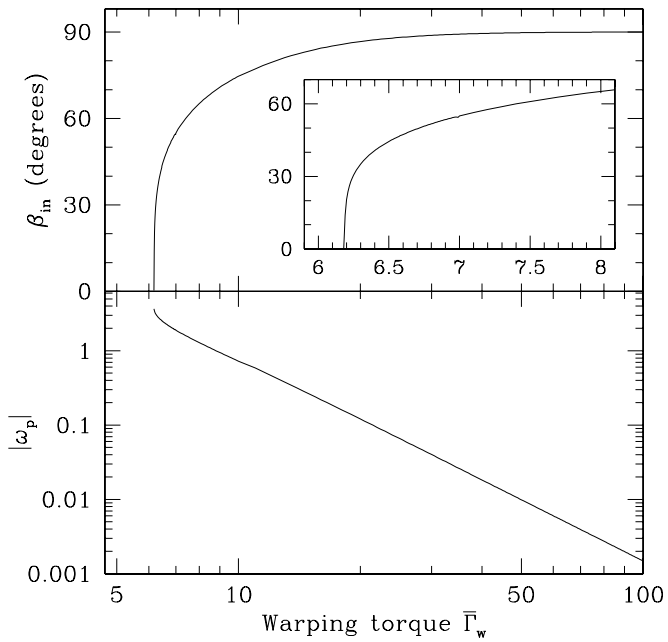

FIG. 4.—Tilt angle at the inner edge of the disk, $\beta_{\rm in}$, and the disk precession frequency $|\boldsymbol{\omega}_p|$ as a function of warping torque parameter $\bar{\Gamma}_w$. The other parameters are fixed to $\bar{\Omega}_p = 10$, $\mathcal{J}_{\rm in} = 1, \eta_0 = 1$, $\beta_1 = \beta_2 = 0.6$, $\sigma_1 = \sigma_2 = 0$, and $D(x) = 1$.

Figure 4 also shows the steady state precession frequency $\boldsymbol{\omega}_p$ as a function of $\bar{\Gamma}_w$. At the onset of warping instability ($\bar{\Gamma}_w \simeq 6.2$), $\boldsymbol{\omega}_p \approx -3.7$. As $\bar{\Gamma}_w$ increases, $|\boldsymbol{\omega}_p|$ drops very rapidly: doubling the warping torque decreases $|\boldsymbol{\omega}_p|$ by roughly a factor of 10. The reason is that for larger $\bar{\Gamma}_w$, the disk tilt is larger (approaching 90° very closely) and the warping region is more extended (see Fig. 5). Note that the surface density of the $\bar{\Gamma}_w = 100$ evolution deviates less from $\sigma_{\rm flat}$ than the one for $\bar{\Gamma}_w = 10$; this is because the local disk-warp is smaller in the former case ($\partial\hat{\boldsymbol{l}}/\partial \ln r \lesssim 0.24$ as compared with $\partial\hat{\boldsymbol{l}}/\partial \ln r \lesssim 0.94$), so that less additional advection is introduced by the warping. The strong dependence of $\boldsymbol{\omega}_p$ on $\bar{\Gamma}_w$ opens the possibility of accounting for a wide variety of low-frequency quasi-periodic oscillations with the nonlinear behavior of a warped disk driven by the magnetic warping instability (see § 5).

We now use equation (21) for the function $D(x)$ and extend the parameter searches to $\bar{\Omega}_p$, $\mathcal{J}_{\rm in}$, and η_0. Figure 6 presents results for different choices of these parameters. For each curve, evolutions were first performed for large $\bar{\Gamma}_w$ until the steady state is reached. Then $\bar{\Gamma}_w$ was gradually lowered so that a sequence of steady state solutions was traced out. (When $\bar{\Gamma}_w$ becomes smaller than a certain critical torque, the disks suddenly flattens completely; see § 4.3.)

Several general features of the steady state disks appear to be robust: In all cases, $\boldsymbol{\omega}_p$ strongly depends on $\bar{\Gamma}_w$. Furthermore, $\beta_{\rm in}$ becomes significant ($\gtrsim 60^\circ$) for $\bar{\Gamma}_w$ even slightly exceeding the critical value for the onset of the warping instability. The precession frequency $\boldsymbol{\omega}_p$ depends strongly on $\bar{\Omega}_p$ as well, as comparison between the $\bar{\Omega}_p = 10$ and $\bar{\Omega}_p = 25$ curves reveals: for the same $\bar{\Gamma}_w$, changing $\bar{\Omega}_p$ by a factor of 2.5 results in a change of $\boldsymbol{\omega}_p$ by about 1 order of magnitude.

Consider now the effect of larger viscosity ratio $\eta_0 = \nu_{20}/\nu_{10}$ [=12.5 and 50, corresponding to $\alpha = 0.2$ and 0.1 in $\nu_2/\nu_1 = 1/(2\alpha^2)$; see § 3.2]. A larger ν_2/ν_1 represents a disk more

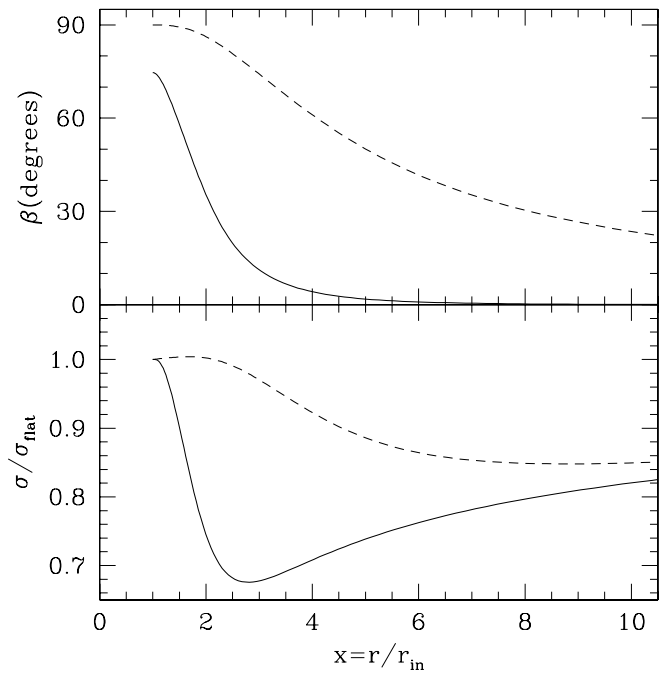

FIG. 5.—Steady-state disk profiles for $\bar{\Gamma}_w = 10$ (*solid lines*) and $\bar{\Gamma}_w = 100$ (*dashed lines*), with the other parameters the same as in Fig. 4. The top panel shows the tilt angle β as a function of radius, the bottom panel the surface density. Note that for $\bar{\Gamma}_w = 100$, the disk is tilted out to larger radii, but the surface density deviates less from that of the flat disk.

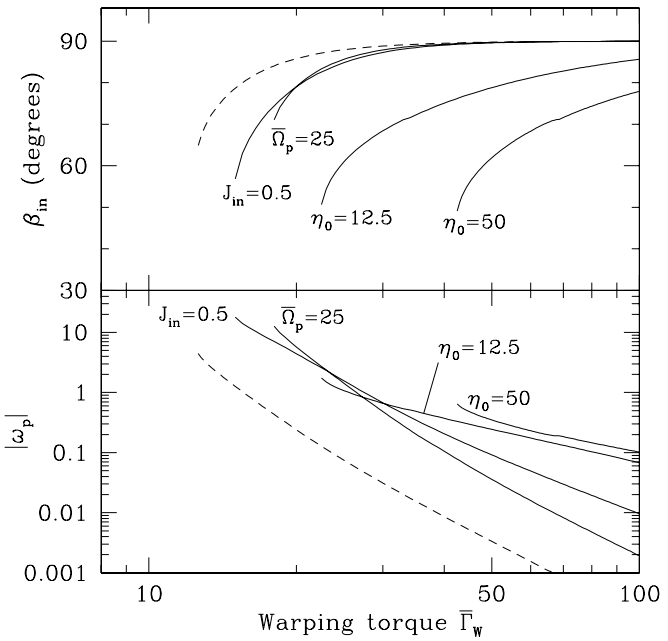

FIG. 6.—Similar to Fig. 4, but for different sets of parameters. The dashed lines correspond to a run with the same parameters as in Fig. 4, $\bar{\Omega}_p = 10$, $\mathcal{J}_{in} = 1$, $\eta_0 = 1$, but with $D(x)$ given by eq. (21). Each one of the remaining runs is obtained by changing the value of one of these parameters, as labeled.

resistive to bending, so that a larger warping torque $\bar{\Gamma}_w$ is required for the magnetic warping instability to operate. In addition, β_{in} approaches 90° more slowly as $\bar{\Gamma}_w$ is increased. Figure 7 shows the steady state disk profiles for the case of $\eta_0 = 50$. These differ appreciably from the profiles obtained with $\eta_0 = 1$ (as shown in Fig. 5): The tilted region of the disk extends to larger radii ($x \approx 20$) for $\eta_0 = 50$ than for $\eta_0 = 1$; the disk is also locally flatter ($\partial \hat{\boldsymbol{l}}/\partial \ln r \lesssim 0.13$) and more depleted (with σ/σ_{flat} being as small as 0.03).

The inner boundary condition is somewhat critical. The disk behavior described above works for relatively large $\mathcal{J}_{in}$ ($\gtrsim 0.2$, depending on the other parameters). However, reducing $\mathcal{J}_{in}$ further leads to singularities in the disk: For evolutions with smaller $\mathcal{J}_{in}$, say, $\mathcal{J}_{in} = 0.1$, it appears that the surface density tends to zero at some finite radius x_{sing} away from the inner edge. The tilt angle β is nonzero inside x_{sing} and close to zero outside x_{sing}. Overall, it appears that the disk pinches off and two regions remain: a flat outer disk with inner boundary at x_{sing} and a strongly tilted, rapidly precessing inner disk inside x_{sing} (which may be viewed as part of the magnetosphere).

4.3. *Discontinuous Behavior: Hystereses*

In Figure 6, the tilt angle β_{in} along each curve does not approach zero continuously as $\bar{\Gamma}_w$ is reduced but exhibits a discontinuity. A closer examination reveals a hysteretic behavior of warp disks.

Consider the $\eta_0 = 12.5$ case in Figure 6 as an example (see Fig. 8). If we start with a slightly perturbed disk ($\beta \ll 1$, $\sigma = \sigma_{flat}$), then the perturbation decays for $\bar{\Gamma}_w < \bar{\Gamma}_{crit,1} \approx 31.3$ and the disk settles down into the flat state. For $\bar{\Gamma}_w$ slightly larger than $\bar{\Gamma}_{crit,1}$, the growth rate of the perturbation is proportional to $\bar{\Gamma}_w - \bar{\Gamma}_{crit,1}$; nonetheless the perturbation grows to large amplitude (with β_{in} reaching $\approx 70°$ in the final steady state). Thus, starting from small perturbations, the disk evolves into a steady state that depends discontinuously on $\bar{\Gamma}_w$ (Fig. 8, *solid line*).

The situation is different if one starts from a highly warped state: We first evolve the disk with $\bar{\Gamma}_w > \bar{\Gamma}_{crit,1}$ until the final (strongly warped) steady state is reached. We then reduce $\bar{\Gamma}_w$ gradually; for each new value of $\bar{\Gamma}_w$ we evolve the disk to a new steady state (using the "previous" steady state solution as the

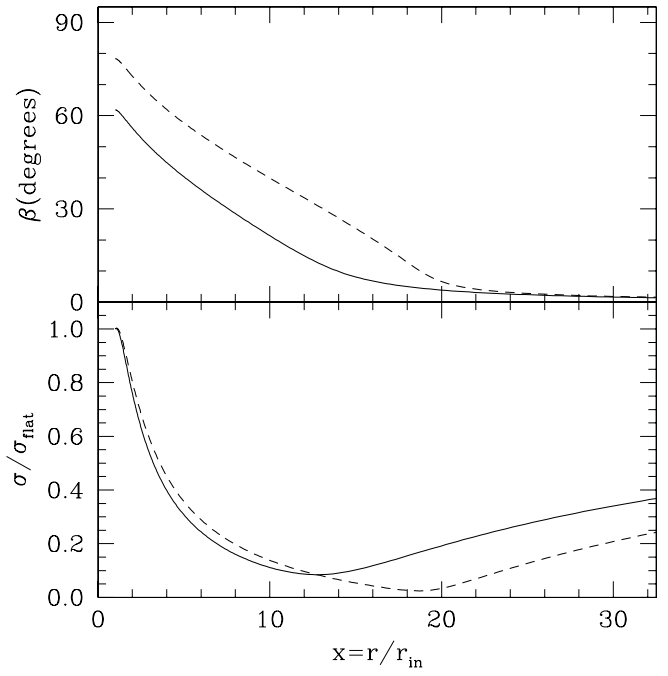

FIG. 7.—Steady state disk profiles for $\bar{\Gamma}_w = 50$ (*solid lines*) and $\bar{\Gamma}_w = 100$, both with $\eta_0 = 50$, $D(x)$ from eq. (21) and the other parameters as in Fig. 4. The top panel shows the tilt angle β as a function of radius, the bottom panel the surface density (cf. Fig. 5).

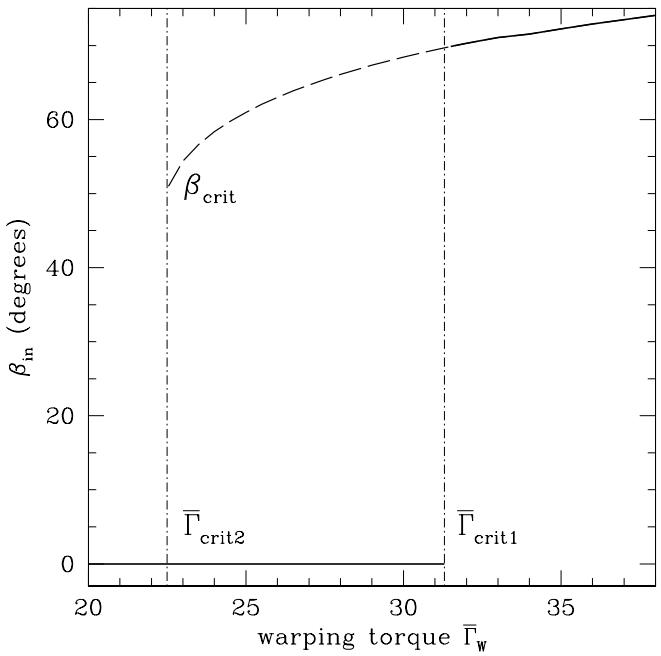

FIG. 8.—Hystereses of warped disks. Plotted is the steady state tilt angle at the inner disk edge as a function of the torque parameter $\bar{\Gamma}_w$. See § 4.3 for details.

initial condition). As long as $\bar{\Gamma}_w > \bar{\Gamma}_{\rm crit,1}$ this procedure produces the same sequence of steady state disks we found when starting from a slightly perturbed disk. However, we find that even below $\bar{\Gamma}_{\rm crit,1}$, there still exits steady state warped disks (see the dashed curve in Fig. 8). We can follow this sequence down to a second critical value $\bar{\Gamma}_{\rm crit,2} \approx 22.5$. Slightly above $\bar{\Gamma}_{\rm crit,2}$, the tilt angle depends on $\bar{\Gamma}_w$ as $\beta_{\rm in} = \beta_{\rm crit} + a(\bar{\Gamma}_w - \bar{\Gamma}_{\rm crit,2})^{1/2}$ for some constant a and $\beta_{\rm crit} \approx 50^\circ$. As we reduce $\bar{\Gamma}_w$ below $\bar{\Gamma}_{\rm crit,2}$, this warped steady state sequence terminates abruptly and the disk relaxes to the flat state.

Thus, for $\bar{\Gamma}_{\rm crit,2} < \bar{\Gamma}_w < \bar{\Gamma}_{\rm crit,1}$, both a flat disk and a warped steady state disk solution exist. The steady state for such a disk depends on the history of the disk. When the disk parameters vary slightly—for example because the accretion rate varies—the disk might switch discontinuously between the two states. As the disk moves across a critical value, a strongly warped disk might suddenly "turn off" and become flat, or a flat disk might suddenly become unstable, with the warp growing to significant values. Since the local disk warp is fairly small at each radius (the maximum $|\partial \hat{\boldsymbol{l}}/\partial \ln r|$ being approximately 0.3), it seems unlikely that the hysteresis is merely an artifact of the adopted simplifying evolution equations (see § 3).

We find that all parameter sets examined in Figure 6 exhibit such a hysteresis (e.g., for $\bar{\Omega}_p = 10$, $\mathcal{J}_{\rm in} = \eta_0 = 1$: $\bar{\Gamma}_{\rm crit,2} \approx 12.5$, $\bar{\Gamma}_{\rm crit,1} \approx 16.9$; for $\bar{\Omega}_p = 25$, $\mathcal{J}_{\rm in} = \eta_0 = 1$: $\bar{\Gamma}_{\rm crit,2} \approx 18$, $\bar{\Gamma}_{\rm crit,1} \approx 38.2$; for $\bar{\Omega}_p = 10$, $\mathcal{J}_{\rm in} = 0.5, \eta_0 = 1$: $\bar{\Gamma}_{\rm crit,2} \approx 15$, $\bar{\Gamma}_{\rm crit,1} \approx 20.3$; for $\bar{\Omega}_p = 10$, $\mathcal{J}_{\rm in} = 1$, $\eta_0 = 50$: $\bar{\Gamma}_{\rm crit,2} \approx 42.5$, $\bar{\Gamma}_{\rm crit,1} \approx 69.7$).

5. DISCUSSION AND CONCLUSION

In this paper we have demonstrated through numerical simulations that accretion disks around magnetic stars can develop into a warped steady state in which the disk attains a fixed (warped) shape and precesses rigidly. This work extends our previous (local and global) linear analysis of magnetically driven warping and precession of accretion disks. We find that whenever the magnetic warping instability criterion is satisfied in the linear regime, the inner disk (close to the magnetosphere boundary) is likely to be highly warped. The steady state precession frequency spans a wide range, depending sensitively on the warping and precession torques (and hence on the parameters of the system).

5.1. *Limitations of the Models*

Before drawing any astrophysical conclusion from our work, it is useful to recall some of the limitations of our models. First, the nonlinear warp equations we adopted in our simulations are based on phenomenological descriptions of viscosities (see § 3). Second, the magnetic torque formulae were derived under several assumptions, e.g., locally flat disk and the use of the free parameter ζ to parameterize the magnetic field twist in quasi-steady state (see § 3). Finally, there are intrinsic uncertainties associated with the inner boundary conditions of the disk. In our problem, the inner boundary is located at the magnetosphere radius, where the transition between a Keplerian disk and a corotating magnetosphere occurs. The physics that determines this transition is obviously complicated (see references cited in § 1). The magnetic warping and precession torques are steep functions of radius and are maximal close to the inner disk edge. Therefore, the details of our numerical results depend sensitively on the physics at the inner radius of the accretion disk. In our calculations we adopted the simplest inner boundary conditions for the disk. A more rigorous resolution of this problem will have to involve studying the coupling of the warped disk and the magnetosphere.

Given these uncertainties and limitations, we cannot be sure whether some of the features we found for the warped disks (such the hysteresis behavior discussed in § 4.3) correspond to reality in any way or simply represent artifacts of our models. Nevertheless, our numerical experiments show that the general behaviors of magnetically driven warped disks that we found (as summarized at the beginning of § 5) are robust.

5.2. *Astrophysical Implications*

The most important feature of magnetically driven disk warping studied in this paper is that the disk naturally evolves into a steady state that is highly warped near the inner radius (the magnetosphere boundary). This is in contrast to other warping mechanisms (e.g., those due to radiation pressure or irradiation-driven disk wind), which operate from the outside in. Such a highly warped disk can lead to modulation of the observed radiation flux either by obscuring the central star or by changing the reprocessed disk emission. As mentioned in § 1, there is growing observational evidence for quasi-periodic oscillations (QPOs) or variabilities in radiation fluxes induced by warped inner disks in various systems, ranging from YSOs (e.g., AA Tauri; see Bouvier et al. 1999) to X-ray binaries (e.g., Her X-1: see Deeter et al. 1998; Scott et al. 2000; see also Shirakawa & Lai 2002b for a list of other X-ray binaries showing mHz QPOs).

Another interesting feature of our models is that the disk can be in either a completely flat state (warping-stable) or a highly warped state. Thus, for a given system, as the disk parameters (e.g., accretion rate) vary, the disk can switch abruptly between the two states, leading to the appearance/disappearance of QPOs (with the corresponding change in radiation flux or spectrum). Indeed, in X-ray binaries, there are many examples in which QPOs occur only in certain spectral states and not in the others (e.g., van der Klis 2000).

Our calculations showed that the steady state precession frequency of the disk can be much smaller (by up to several orders of magnitude, depending on the system parameters; see Fig. 6) than the frequency of the linear mode; the latter was approximately equal to the precession frequency at the inner radius of the disk (see Shirakawa & Lai 2002a, 2002b for typical numbers for X-ray binaries). Thus, for magnetized neutron stars (with surface magnetic field $\sim 10^{12}$ G), the global precession frequency is

$$\nu_p = A\frac{\Omega_p(r_{\rm in})}{2\pi} = -(1.2\ {\rm mHz}) A \mu_{30}^2 M_{1.4}^{-1/2} r_8^{-11/2} \Sigma_4^{-1} D^{-1} \sin^2\theta, \quad (25)$$

where the dimensionless parameter A can be much smaller than unity, and $\mu_{30} = \mu/(10^{30}\ {\rm G\ cm^3})$, $M_{1.4} = M/(1.4\ M_\odot)$, $\Sigma_4 = \Sigma(r_{\rm in})/(10^4\ {\rm g\ cm^{-2}})$, with $r_8 = r_{\rm in}/(10^8\ {\rm cm}) = 3.4\eta^{4/7}\mu_{30}^{4/7} M_{1.4}^{-1/7} \dot{M}_{17}^{-2/7}$ as well as $\dot{M}_{17} = \dot{M}/(10^{17}\ {\rm g\ s^{-1}})$. For typical parameters appropriate for T Tauri stars, the precession period is given by

$$\nu_p^{-1} = \frac{2\pi}{A\Omega_p(r_{\rm in})} = -(124\ {\rm yr}) A^{-1} B_3^{-2} R_2^{-6} M_1^{1/2} \left(\frac{r_{\rm in}}{8\ R_\odot}\right)^{11/2} \Sigma_3 D (\sin\theta)^{-2}, \quad (26)$$

where $B = \mu/R^3 = 10^3 B_3$ G is the surface magnetic field of the star, $R = (2R_\odot)R_2$ is the stellar radius, and $M_1 = M/(1\ M_\odot)$. Therefore magnetically driven precession can potentially explain some long-period QPOs/variabilities in X-ray binaries and YSOs.[4] It is of interest to note that the magnetically driven precession is retrograde, as observed in some systems (e.g., Her X-1).

Finally, if the outflows from YSOs are produced from interaction between the stellar magnetic field and the disk, as in the X-wind models (Shu et al. 1994), then the magnetic effects studied in this paper may be responsible for the jet precession observed in several systems (see Terquem et al. 1999 and references therein; see also Lai 2003 for possible warping instability in magnetically driven disk outflows).

[4] We have only included the magnetic torques in our calculations. In real astrophysical systems, there may be other torques that contribute to (or even dominate) the disk precession; for example, the tidal torque in binary systems (e.g., Papaloizou & Terquem 1995; Terquem et al. 1999) and the torque associated with general relativistic frame dragging effect in low-mass X-ray binaries (see Shirakawa & Lai 2002a). Note that even in those systems where other torques dominate disk precession, the magnetic warping torque studied here can still be important in exciting/maintaining the disk tilt.

This work has been supported in part by NSF grants AST 99-86740, AST 03-07252, and PHY 99-00672 and NASA grant NAG5-12034.

APPENDIX

NUMERICAL METHOD

Equations (16) and (17) are essentially of the form

$$\frac{\partial \sigma}{\partial \tau} - A\frac{\partial^2 \sigma}{\partial x^2} - B\frac{\partial \sigma}{\partial x} = C, \tag{A1}$$

$$\frac{\partial \boldsymbol{l}}{\partial \tau} - D\frac{\partial^2 \boldsymbol{l}}{\partial x^2} - E\frac{\partial \boldsymbol{l}}{\partial x} = \boldsymbol{F}, \tag{A2}$$

with coefficients $A, \ldots, \boldsymbol{F}$ depending nonlinearly on the variables σ and $\boldsymbol{l}$ (for ease of notation, we omit the hat on $\hat{\boldsymbol{l}}$ here). We discretize these equations using the Crank-Nicholson method (Press et al. 1992). Time derivatives are discretized as usual; for example,

$$\left(\frac{\partial \sigma}{\partial \tau}\right)_i \rightarrow \frac{\bar{\sigma}_i - \sigma_i}{\Delta \tau}. \tag{A3}$$

The index i labels the spatial grid points, unbarred quantities like σ_i denote values at the current time τ_0 (which are known), and barred quantities denote values at the new time $\tau_0 + \Delta\tau$, which are to be determined. Spatial derivatives are averaged over τ_0 and $\tau_0 + \Delta\tau$, for example

$$\left(A\frac{\partial^2 \sigma}{\partial x^2}\right)_i \rightarrow -\frac{A_i}{2}\frac{\sigma_{i+1} - 2\sigma_i + \sigma_{i-1}}{(\Delta x)^2} - \frac{\bar{A}_i}{2}\frac{\bar{\sigma}_{i+1} - 2\bar{\sigma}_i + \bar{\sigma}_{i-1}}{(\Delta x)^2}. \tag{A4}$$

Here, A_i is computed using the known values at τ_0, whereas $\bar{A}_i$ is a function of the desired values at $\tau_0 + \Delta\tau$. This discretization leads to a nonlinear system of equations, which is solved iteratively. We start with a guess for σ and $\boldsymbol{l}$ at time $\tau_0 + \Delta\tau$, which we denote with tildes: $\tilde{\sigma}_i$, $\tilde{\boldsymbol{l}}_i$. Based on these guesses, we compute coefficients $\tilde{A}_i, \ldots, \tilde{F}_i$. Now, we discretize spatial derivatives like in equation (A4), using $\tilde{A}_i$ instead of $\bar{A}_i$:

$$\left(A\frac{\partial^2 \sigma}{\partial x^2}\right)_i \rightarrow -\frac{A_i}{2}\frac{\sigma_{i+1} - 2\sigma_i + \sigma_{i-1}}{(\Delta x)^2} - \frac{\tilde{A}_i}{2}\frac{\bar{\sigma}_{i+1} - 2\bar{\sigma}_i + \bar{\sigma}_{i-1}}{(\Delta x)^2}. \tag{A5}$$

Substituting these difference expressions into equations (A1) and (A2) now yields *linear* tridiagonal systems of equations for $\bar{\sigma}_i$ and $\bar{\boldsymbol{l}}_i$. Solving these yields improved values $(\bar{\sigma}_i,\ \bar{\boldsymbol{l}}_i)$ for the variables at the next time step, which are used in place of $(\tilde{\sigma}_i,\ \tilde{\boldsymbol{l}}_i)$. We iterate this process until convergence.

This scheme is computationally more expensive per time step than an explicit method. However, it is second-order accurate in time and unconditionally stable, so that one can take very large time steps. In practice, we often exceed Courant factors of 1000. These large time steps are especially important during the slow relaxation toward a coherently rotating steady state disk. In such a case, one is primarily interested in the time-independent final state, whereas the transient evolution toward this state is less important.

The code uses an adaptive time step: $\Delta\tau$ is adjusted such that the difference in solution at τ_0 and $\tau_0 + \Delta\tau$ is smaller than some threshold, typically 10^{-4}. Furthermore, the code can be used with different radial distributions of grid points, for example linearly or logarithmically spaced grid points. This is done via a mapping $\bar{x} \rightarrow x = x(\bar{x})$, which relates a "computational" coordinate $\bar{x}$ (in which the grid is uniform) to the "physical" radial coordinate x. Rewriting "physical" derivatives in terms of the computational coordinate $\bar{x}$,

$$\frac{\partial}{\partial x} = \frac{\partial \bar{x}}{\partial x}\frac{\partial}{\partial \bar{x}}, \qquad \frac{\partial^2}{\partial x^2} = \left(\frac{\partial \bar{x}}{\partial x}\right)^2 \frac{\partial^2}{\partial \bar{x}^2} + \frac{\partial^2 \bar{x}}{\partial x^2}\frac{\partial}{\partial \bar{x}},$$

shows that the coefficients $A, \ldots, \boldsymbol{F}$ will be modified by this mapping, however, the principal structure of equations (A1) and (A2) does not change. Usually, logarithmically spaced grid points are used, which accurately resolve the fine structure close to the inner edge while allowing to move the outer boundary far out, typically to $x_{\rm out} = 1000$.

We verified that our code is second-order convergent in space and time and recovers the standard flat disk solution, equation (13), in the absence of warping/precession torques. Section 4.1 confirms that in the linear regime our code recovers the linear stability analysis of Shirakawa & Lai (2002b).

REFERENCES

Aly, J. J. 1980, A&A, 86, 192
Aly, J. J., & Kuijpers, J. 1990, A&A, 227, 473
Anzer, U., & Börner, G. 1980, A&A, 83, 133
———. 1983, A&A, 122, 73
Bate, M. R., et al. 2000, MNRAS, 317, 773
Bouvier, J., et al. 1999, A&A, 349, 619
Campbell, C. G. 1997, Magnetohydrodynamics in Binary Stars (Dordrecht: Kluwer)
Carpenter, J. M., Hillenbrand, L. A., & Skrutskie, M. F. 2001, AJ, 121, 3160
Deeter, J. E., et al. 1998, ApJ, 502, 802
Fendt, C., & Elstner, D. 2000, A&A, 363, 208
Ghosh, P., & Lamb, F. K. 1979, ApJ, 234, 296
Goodson, A. P., Winglee, R. M., & Böhm, K.-H. 1997, ApJ, 489, 199
Hayashi, M. R., Shibata, K., & Matsumoto, R. 1996, ApJ, 468, L37
Lai, D. 1998, ApJ, 502, 721
———. 1999, ApJ, 524, 1030
———. 2003, ApJ, 591, L119
Lipunov, V. M., & Shakura, N. I. 1980, Soviet Astron. Lett., 6, 14
Lovelace, R. V. E., Romanova, M. M., & Bisnovatyi-Kogan, G. S. 1995, MNRAS, 275, 244
———. 1999, ApJ, 514, 368
Maloney, P. R., Begelman, M. C., & Nowak, M. A. 1998, ApJ, 504, 77
Miller, K. A., & Stone, J. M. 1997, ApJ, 489, 890
Ogilvie, G. I. 1999, MNRAS, 304, 557
Ogilvie, G. I., & Dubus, G. 2001, MNRAS, 320, 485
Papaloizou, J. C., & Lin, D. N. C. 1995, ApJ, 438, 841
Papaloizou, J. C., & Pringle, J. E. 1983, MNRAS, 202, 1181
Papaloizou, J. C., & Terquem, C. 1995, MNRAS, 274, 987
Press, W. H., Teukolsky, S., Vetterling, W. T., & Flannery, B. P. 1992, Numerical Recipes in C: The Art of Scientific Computing (2nd ed.; Cambridge: Cambridge Univ. Press)
Priedhorsky, W. C., & Holt, S. S. 1987, Space Sci. Rev., 45, 291
Pringle, J. E. 1992, MNRAS, 258, 811
———. 1996, MNRAS, 281, 357
Pringle, J. E., & Rees, M. J. 1972, A&A, 21, 1
Quillen, A. C. 2001, ApJ, 563, 313
Romanova, M. M., et al. 2003, ApJ, 588, 400
Schandl, S., & Meyer, F., 1994, A&A, 289, 149
Scott, D. M., Leahy, D. A., & Wilson, R. B. 2000, ApJ, 539, 392
Shirakawa, A., & Lai, D. 2002a, ApJ, 564, 361
———. 2002b, ApJ, 565, 1134
Shu, F. H., et al. 1994, ApJ, 429, 781
Spruit, H. C., & Taam, R. E. 1993, ApJ, 402, 593
Terquem, C., Eislöffel, J., Papaloizou, J. C. B., & Nelson, R. P. 1999, ApJ, 512, L131
Terquem, C., & Papaloizou, J. C. B. 2000, A&A, 360, 1031
Terquem, C. E. J. M. L. J. 1998, ApJ, 509, 819
van Ballegooijen, A. A. 1994, Space Sci. Rev., 68, 299
van der Klis, M. 2000, ARA&A, 38, 717
Wang, Y.-M. 1987, A&A, 183, 257
———. 1995, ApJ, 449, L153
Wijers, R. A. M. J., & Pringle, J. E., 1999, MNRAS, 308, 207